Positional accuracy of novel x-ray-image-based dynamic tumor-tracking irradiation using a gimbaled MV x-ray head of a vero4DRT (MHI-TM2000)

Nobutaka Mukumoto[1], Mitsuhiro Nakamura[1], Akira Sawada*[1,2], Kunio Takahashi[1,3], Yuki Miyabe[1], Kenji Takayama[4], Takashi Mizowaki[1], Masaki Kokubo[5], and Masahiro Hiraoka[1]

[1]Department of Radiation Oncology and Image-applied Therapy, Graduate School of Medicine, Kyoto University, Kyoto 606-8507, Japan

[2]Department of Radiological Technology, Faculty of Medical Science, Kyoto College of Medical Science, Kyoto 622-0041, Japan

[3]Medical Systems Engineering Section, Mitsubishi Heavy Industries Ltd.

[4]Department of Radiology, Kobe City Medical Center General Hospital, Kobe 650-0046, Japan

[5]Division of Radiation Oncology, Institute of Biomedical Research and Innovation, Kobe 650-0047, Japan

***Corresponding author**: Akira Sawada, P_H.D., Graduate School of Medicine, Kyoto University, 54 Kawahara-cho, Shogoin, Sakyo-ku, Kyoto, 606-8507, Japan.

Tel.: +81-75-751-3762; Fax: +81-75-771-9749; E-mail: asawada@kuhp.kyoto-u.ac.jp

Running title: Positional accuracy of x-ray-image-based dynamic tumor-tracking irradiation

25

Conflicts of interest: This research was in part sponsored by Mitsubishi Heavy Industries, Ltd., Japan. Takashi Mizowaki, Masaki Kokubo, and Masahiro Hiraoka have consultancy agreement with Mitsubishi Heavy Industries, Ltd., Japan.

30

Meeting presentation: This research was presented, in part, at the 2011 Joint the American Association of Physicists in Medicine (AAPM) and the Canadian Organization of Medical Physicists (COMP) Meeting in Vancouver, July 31 – August 4, 2011.

Abstract

Purpose: To verify the positional accuracy of a novel x-ray-image-based dynamic tumor-tracking (DTT) irradiation technique using the gimbaled MV x-ray head of a vero4DRT (MHI-TM2000).

Methods and Materials: Verification of the x-ray-image-based DTT was performed using three components: a three-dimensional moving phantom with a steel ball target, a laser displacement gauge, and an orthogonal kV x-ray imaging subsystem with a gimbaled MV x-ray head and the system controller of the vero4DRT. The moving phantom was driven based on seven periodic patterns (peak-to-peak amplitude [A]: 20-40 mm, breathing period [T]: 2–5 s) and 15 patients' aperiodic respiratory patterns (A: 6.5–22.9 mm, T: 1.9–5.8 s). The target position was detected in real time with the orthogonal kV x-ray imaging subsystem using the stereo vision technique. Subsequently, the vero4DRT predicted the next position of the target, and then the gimbaled MV x-ray head tracked the corresponding orientation of the target. The displacements of the target were measured synchronously using the laser displacement gauge. The difference between the target positions predicted by the vero4DRT and those measured by the laser displacement gauge was computed as the prediction error (E_P), and the difference between the target positions tracked by the gimbaled MV x-ray head and predicted target positions as the mechanical error (E_M). Total tracking system error (E_T) was defined as the difference between the tracked and measured target positions.

Results: The root mean squares (RMSs) of E_P, E_M, and E_T were up to 0.8, 0.3, and 0.7 mm, respectively, for the periodic patterns. Regarding the aperiodic patterns, the median RMSs of E_P, E_M, and E_T were 1.2 (range, 0.9–1.8) mm, 0.1 (range, 0.1–0.5) mm, and 1.2 (range, 0.9–1.8) mm, respectively. From the results of principal component

analysis, tracking efficiency, defined as the ratio of twice the RMS of E_T to A, was improved for patients with high respiratory function ($R = 0.91$; $p < 0.01$).

Conclusions: The present study demonstrated that the vero4DRT is capable of high-accuracy x-ray-image-based DTT. E_T was caused primarily by E_P, and E_M was negligible. Furthermore, principal component analysis showed that tracking efficiency could be improved with this system, especially for patients with high respiratory function.

Key words: four-dimensional image-guided radiotherapy, dynamic tumor-tracking irradiation, intrafractional respiratory motion, gimbaled MV x-ray head, tracking accuracy.

I. INTRODUCTION

Several anatomical structures, including the lungs and pancreas, are known to move with breathing.[1] Without management of respiratory motion during radiation therapy, intrafractional respiratory motions during dose delivery lead to blurred dose distributions and an enlarged beam penumbra at the radiation field edge[2,3], resulting in unintended underdosage to the tumor or overdosage to normal tissues.[1,4]

Techniques have been proposed to reduce the impact of respiratory motion, including motion encompassing, respiratory gating, breath holding, forced shallow breathing, and dynamic tumor-tracking (DTT).[1] In the motion-encompassing technique, the mean position and the range of tumor motion are estimated from fluoroscopy or four-dimensional (4D) computed tomography data to define the internal target volume (ITV). However, a large internal margin is required to accommodate tumor motion, which may lead to an increase in normal tissue complications.[5] Respiratory gating, breath holding, and forced shallow breathing can each reduce the size of the ITV, although these techniques are often time-consuming or burdensome for patients. DTT techniques reposition the radiation beam dynamically according to the target's changing position, which can reduce the size of the ITV without prolonging treatment time. To perform DTT techniques, multiple markers need to be implanted in or near the tumor. Although this implantation can sometimes cause complications such as pneumonitis or pneumothorax,[6] the benefits from the use of DTT may outweigh the additional burden on patients.

We developed a novel 4D image-guided radiotherapy (IGRT) system with a DTT function, the vero4DRT (MHI-TM2000; Mitsubishi Heavy Industries, Ltd., Japan, and BrainLAB, Feldkirchen, Germany).[7–13] The system is composed of a 6-MV C-band linear accelerator mounted on an x-ray head with a gimbal mechanism that allows irradiation

while tracking a moving tumor. We have previously reported that the vero4DRT had remarkable accuracy with regard to the stability and reproducibility of the multileaf collimator (MLC) position when swinging the gimbaled MV x-ray head[10] and significantly reduced motion-blurring effects in the dose distribution during the DTT irradiation.[11] Recently, two approaches to DTT irradiation using the vero4DRT have been developed: x-ray image-based and surrogate signal-based DTT. Depuydt *et al.* [14] demonstrated that the vero4DRT was able to track a moving target accurately with the surrogate signal-based DTT technique. In the present study, the positional accuracy of x-ray image-based DTT irradiation was verified.

II. MATERIALS AND METHODS

II. A. System description of the DTT function in the vero4DRT

The vero4DRT has several unique components allowing DTT irradiation, including the compact C-band 6-MV x-ray head with a gimbal mechanism and the gantry-mounted orthogonal kV x-ray imaging subsystem, consisting of two sets of x-ray tubes and flat-panel detectors (FPDs) with a spatial resolution of 0.2 mm.[13] The gimbaled MV x-ray head can rotate along two orthogonal gimbals (pan and tilt rotations) up to ±2.5° with a maximum rotational speed of 9°/s, which can swing the beam up to ±41.9 mm with a maximum speed of 152 mm/s in each direction from the isocenter on the isocenter plane, perpendicular to the beam axis.[10] The stationary accuracy of the gimbaled MV x-ray head is within 0.1 mm at any point within the 40 × 40-mm area around the isocenter.[7]

II. B. Sequential prediction model

In the x-ray image-based DTT irradiation, the target's position can be detected using the orthogonal kV x-ray fluoroscopic images. However, a time delay of 66 ms was observed in the kV x-ray imaging subsystem due to image processing.[7] To compensate for this time delay, the next position of the target was predicted from the previous position sequence of the target, using the following sequential prediction model:

$$x(t) = \sum_{i=1}^{n} (a_x^m x(t-i)) + \varepsilon_x^m(t),$$

and similarly for $y(t)$ and $z(t)$. Here, $x(t)$ is the predicted position of the target, n is the number of data to update the sequential prediction model, a^m is the m^{th} order prediction coefficient of the target, and $\varepsilon^m(t)$ is the m^{th} order residual error of the predicted position of the target. The optimal a^m is determined by minimizing the $\varepsilon^m(t)$ using the Levinson–Durbin algorithm[15,16] for a model-building time period. In the present study, the model-building time period was set at 40 s, and a^m was sequentially updated from the previous 150 consecutive positions (n = 150).

II. C. Experimental system to verify tracking accuracy

A photograph of the experimental system for the verification of the x-ray image-based DTT is shown in Fig. 1. The system comprised a 3D moving phantom with a steel ball target of 9.5 mm in diameter, a laser displacement gauge with positional accuracy of 0.05 mm, the orthogonal kV x-ray imaging subsystem, consisting of two sets of x-ray tubes and FPDs, the gimbaled MV x-ray head, and a system controller of the vero4DRT. In these experiments, the gantry angle was set at 0°.

A schematic diagram of the data flow for the verification of the x-ray

image-based DTT is shown in Fig. 2(a). First, the 3D moving phantom was driven based on the input signals described in II. D with high precision, of 0.1 mm.[17] Subsequently, the current position of the target was independently measured by the laser displacement gauge every 10 ms along the superior–inferior (SI) direction and recorded on the system controller as the measured position of the target. Simultaneously, the 3D target's position was calculated from a pair of two-dimensional (2D) target positions on FPD images using a stereo vision technique every 70 ms. Each of the 2D target positions on the FPD images was detected using the template matching technique. In this experiment, imaging parameters of the kV x-ray tubes were set at 70 kVp, 100 mA, and 5 ms per shot. To compensate for the time delay in image processing by the kV x-ray imaging subsystem, the next position of the target was predicted from the previous position sequence of the target using the sequential prediction model described in II. B. The prediction error (E_P) was defined as $E_p = y_p - y_m$, where y_p is the target position predicted by the sequential prediction model and y_m is the target position measured by the laser displacement gauge. Next, the corresponding orientation of the predicted target was transferred to the gimbaled MV x-ray head, and then the gimbaled MV x-ray head tracked the target by pan and tilt rotations. However, this process generates a 5-ms response delay in the gimbaled MV x-ray head, leading to a mechanical error (E_M), defined as $E_M = y_t - y_p$, where y_t is the target position tracked by the gimbaled MV x-ray head. The predicted and tracked positions of the target were recorded on the system controller every 5 ms.

The geometric point of the tracked target position indicated by the gimbaled MV x-ray head with a tilt rotation angle of $\theta°$ at any given time is illustrated in Fig. 2(b). In this case, the target was moving in the inferior direction, and the predicted target position was inferior to the measured target position. Additionally, the tracked target position

indicated by the gimbaled MV x-ray head did not reach the predicted target position. The orientation of the predicted target at the gantry angle of 0° was calculated using the following equation:

$$\theta_p = -\frac{180}{\pi}\mathrm{atan}\left(\frac{y_p}{960 - z_p}\right),$$

where θ_p is the tilt rotation angle of the gimbaled MV x-ray head indicating the orientation of the predicted target, y_p is the target position predicted by the sequential prediction model in SI direction, and z_p is the target position predicted by the sequential prediction model in anterior–posterior (AP) direction. The vero4DRT tracks the target position at the depth of the existing target along the beam axis by rotating the orthogonal gimbaled MV x-ray head. The tracked target position was also determined using the following equation:

$$y_t = -(960 - z_d)\tan\left(\frac{\theta_t}{180}\pi\right),$$

where y_t is the target position tracked by the gimbaled MV x-ray head in SI direction, z_d is the target position detected by the orthogonal kV x-ray imaging subsystem in AP direction, and θ_t is the tilt rotation angle of the gimbaled MV x-ray head indicating the orientation of the tracked target. The total tracking system error (E_T) was expressed as $E_T = y_t - y_m$.

The root mean square (RMS) of the absolute difference for each error was calculated as the representative value. Tracking accuracies in patients were also estimated as a function of respiratory characteristics. To explain the respiratory characteristics, principal component analysis (PCA) was used. PCA is a mathematical algorithm that reduces the dimensionality of the data while retaining most of the variation in the data

set,[18] which is used to identify underlying factors that explain the pattern of correlations within a set of observed variables. Motion characteristics, including peak-to-peak amplitude (A), breathing period (T), and the autocorrelation coefficient with 1T lag (AC) of the target motion were used as the variables. The Kaiser Criterion (eigenvalues > 1.0) was used to extract the components.[19] The principal component score, computed by multiplying the principal component coefficients with each of the motion characteristics, represented the contribution coefficient of the original variables to the new variables.

II.D Characteristics of the motion patterns

To quantify the positional accuracy of the DTT, the following periodic and aperiodic respiratory patterns were used as input respiratory signals of the 3D moving phantom: four 1D sinusoidal patterns (A: 20–40 mm, T: 2–4 s) in the SI direction, three 2D circular patterns (A: 20–40 mm, T: 2–5 s) on the plane perpendicular to the beam axis, and 15 3D patients' respiratory patterns. For the 3D respiratory patterns, A and T were in the range of 6.5 to 22.9 mm and 1.9 to 5.8 s, respectively. The motion patterns are listed in Table I.

III. RESULTS AND DISCUSSION

III.A. Periodic patterns

Variations in the measured and tracked positions of the target for sinusoidal patterns with (a) (A, T) = (40 mm, 2 s), (b) (A, T) = (20 mm, 4 s), and circular patterns with (c) (A, T) = (40 mm, 2 s), and (d) (A, T) = (20 mm, 5 s) are shown in Fig. 3. The gimbaled MV x-ray head tracked the target with high accuracy in real time. The RMS of each error

is shown in Table II. The RMS of E_T ($RMSE_T$) was up to 0.7 mm for the sinusoidal patterns and 0.2 mm for the circular patterns. The largest $RMSE_T$ was observed in the sinusoidal pattern with (A, T) = (40 mm, 2 s). For the sinusoidal pattern of the largest A and the shortest T, (A, T) = (40 mm, 2 s), the alignment errors between the measured and tracked positions of the target would not be compensated for in real time because of the large displacements per unit time. However, the $RMSE_T$ for the sinusoidal pattern of the smallest A and the longest T, (A, T) = (20 mm, 4 s), was 0.2 mm, comparable to the spatial resolution of 0.20 mm for the FPD. Even for the sinusoidal pattern of the smallest A and the longest T, the velocity was faster than clinically observed respiration variations, as several investigators have reported.[1,20,21] Meanwhile, E_P was smaller for the circular patterns than for the sinusoidal patterns. Even in the circular pattern of the largest A and the shortest T, (A, T) = (40 mm, 2 s), the gimbaled MV x-ray head tracked the current position of the target with high accuracy ($RMSE_T$ = 0.2 mm). The predictions of the circular patterns were easier than those of the sinusoidal patterns because the circular patterns had constant velocity.

III.B. Aperiodic patterns

Motion characteristics and the RMS of E_P, E_M, and E_T for 3D respiratory patterns are summarized in Table III. The median RMSs of E_P, E_M, and E_T were 1.2 (range, 0.9–1.8) mm, 0.1 (range, 0.1–0.5) mm, and 1.2 (range, 0.9–1.8) mm, respectively. As with the one-dimensional (1D) sinusoidal and 2D circular periodic patterns, the values of E_M were small enough to track the target with high mechanical precision. However, E_P for the 3D respiratory patterns increased due to complex respiratory motion, such as hysteresis trajectory (the difference between the inhalation and exhalation trajectory of

the tumor)[22] or deep respiration. Variations in the measured and tracked positions of the target for representative regular and irregular respiratory cases are shown in Figures 4(a) and 4(b), respectively. As indicated by the *AC* of the target motion and standard deviation (SD) of *A* and *T* in Table III, case nos. 8 and 4 were defined as representative regular and irregular respiratory patterns, respectively. The *A* and *T* varied constantly per breath, indicating that acceleration and velocity also changed by the second. At the end-inspiration or end-expiration phases, the vero4DRT had to predict the turning points by monitoring the change in acceleration and velocity, making the prediction of the target's position difficult, especially for the irregular respiratory patterns.

Probability histograms as a function of the alignment error with or without tracking for regular and irregular respiratory cases are shown in Figures 4(c) and 4(d), respectively. The RMS of the alignment error for the regular respiratory case decreased, from 5.0 mm without tracking to 0.9 mm with tracking, and that for the irregular respiratory case decreased, from 9.3 mm without tracking to 1.3 mm with tracking. Compared with the non-tracking state, the alignment error between the target and gimbaled MV x-ray head was markedly reduced with tracking for both regular and irregular respiratory patterns.

The characteristics of respiratory patterns, including *A*, *T*, and *AC*, can be explained by PCA. Table IV summarizes the principal components and their coefficients. Each of the original parameters was standardized with a mean of 0 and variance of 1. Among the three principal components, the first principal component that was extracted explained 64.8% of the total variance. Since the principal component coefficients of *A*, *T*, and *AC* had negative sign, the principal component score became smaller with a combination of larger *A*, longer *T*, and higher *AC*. Generally, the amount of ventilation is

larger for the patient with a combination of larger A and longer T. Moreover, patients with larger volume of ventilation and higher AC have high respiratory function. Figure 5 shows variations in the tracking efficiency, defined as the ratio of twice the $RMSE_T$ to A, as a function of principal component scores. A strong positive correlation was observed between tracking efficiency and the principal component score ($R = 0.91$; $p < 0.01$), indicating that the vero4DRT can track a moving tumor with high accuracy for patients with high respiratory function (*i.e.*, a low principal component score for respiratory motion).

III.C. Comparison with other DTT irradiation techniques

Several DTT irradiation techniques have been developed. The dynamic MLC (DMLC) tumor-tracking system has been experimentally investigated on several linear accelerators to compensate for tumor motion.[23–29] The CyberKnife (Accuray, Sunnyvale, CA) can also track a target by continuously monitoring internal tumor motion with two sets of static kV x-ray imaging subsystems (Xsight) or by monitoring three respiratory surrogate markers, fixed to a form-fitting vest with a stereo camera system (Synchrony).[30–34] Table V shows a comparison of the characteristics of various DTT techniques.[26,32,33] The RMS of tracking accuracy according to the DMLC-based tracking system for the 3D aperiodic motion patterns was < 1.5 mm, excluding the prediction-model-building time period, and < 2.5 mm including it.[26] Assessment of tracking accuracy of the CyberKnife revealed a RMS of 1.1 mm for the periodic motion patterns and showed a SD of 0.2–2.5 mm for the aperiodic motion patterns.[32,33] The RMSs in the present study were comparable to those in other DTT irradiation techniques. However, the DMLC-based tracking system has a single kV x-ray imaging subsystem and

requires a non-tracking period of 6 s after the MV beam starts to construct a prediction model.[26] In the case when the tumor or some markers cannot be identified on electronic portal imaging device images due to a location outside the radiation field or interruption of MV beam delivery, the prediction time is prolonged.[27,28] The prediction accuracy can be affected by unintended respiratory motions, such as coughing, or deep respiration, with loss of target information necessary for 3D localization. Additionally, the accuracy of this system is limited by the maximum leaf speed and the finite leaf width.[29] To manage respiratory motion, DMLC tracking will require more rapid control of MLCs than the maximum leaf speed used in DMLC-based intensity modulated radiation therapy, which may cause tracking failure. Also, due to the low beam efficiency, Xsight results in an unacceptable additional radiation dose for the patient when tumor position is monitored in real time for an extended treatment time. It is possible that Synchrony can overcome the imaging dose limitation; however, an extended treatment time leads to miscorrelation between the external surrogate and internal tumor.[34] The DTT irradiation technique presented also requires continuous kV imaging. The imaging dose for setup verification on the kV x-ray imaging system in the vero4DRT was similar to the dose reported for other IGRT systems.[35–38] However, continuous monitoring with the kV imaging subsystem may have resulted in an additional imaging dose to the patient. The imaging dose required to monitor the target should be kept as low as reasonably achievable by adjusting imaging parameters.

III.D. Limitations

The present study has several limitations. First, the tracked target of the 3D moving phantom was an unsheltered steel ball. The target could be considered as a model

lung tumor or markers implanted in or near the tumor for easy detection on radiographic images. In clinical practice, however, body anatomy such as rib bones, the spine, or mediastinum could prevent detection of the tumor or markers. As the target was clearly visible for the present experiment, there were almost no detection errors. The realistic tracking accuracy in a patient would be decreased by anatomical limitations. Second, the vero4DRT cannot correct the respiratory motion along the AP direction at a gantry angle of 0° because the gimbaled MV x-ray head rotates along pan and tilt direction which are parallel to the axes in the left–right (LR) and SI directions. According to a report published by the American Association of Physicists in Medicine (AAPM) task group 76[1], the peak-to-peak amplitude of lung tumor motion was typically less than 10 mm in the AP direction. Prior to this study, we simulated the dosimetric error with displacements along the beam axis. Figure 6 shows the diagram of the simulation and variations of the mean dose in the planning target volume (PTV) under the conditions of the displacements along the beam axis. The PTVs of 30 mm in diameter located at the displacements of -5, 0, and 5 mm from the isocenter with source-to-isocenter distance of 1000 mm were simulated under the condition of the one uniform field port adding 5-mm MLC margin. Dose calculation was performed under the same monitor unit with variance of 1% and a grid size of 2.3 x 2.3 x 2.5 mm^3 using X-ray Voxel Monte Carlo of well-commissioned 6 MV photon beam on a radiation treatment planning system (iPlan; BrainLAB, Germany). It was found that the dosimetric error of the PTV mean dose was within ±3% at a displacement of ±5 mm from the isocenter. Thus, the dosimetric impact of displacements along the beam axis would be cancelled out with multiple ports under the moving condition, although the gimbaled MV x-ray head cannot track a target along the beam axis. Finally, we measured the position of the target only in the SI direction with the laser

displacement gauge due to a structural issue. Given the small motion amplitude and regularity of respiratory patterns in the LR and AP directions, however, the tracking error in directions other than the SI would be either equal or smaller than those in the SI direction.

IV. CONCLUSIONS

We demonstrated the positional accuracy of x-ray image-based DTT irradiation using the gimbaled MV x-ray head of the vero4DRT. The RMSs of E_P, E_M, and E_T for the periodic patterns were up to 0.8 mm, 0.3 mm, and 0.7 mm, respectively. For the aperiodic patterns, the RMSs of E_P, E_M, and E_T ranged from 0.9 to 1.8 mm, from 0.1 to 0.5 mm, and from 0.9 to 1.8 mm, respectively. The vero4DRT is capable of tracking a moving target with high accuracy even for aperiodic patterns. Additionally, principal component analysis showed that tracking efficiency could be improved with this system, especially for patients with high respiratory function.

ACKNOWLEDGMENTS

We express our appreciation to the entire technical staff at MHI for providing detailed information on the gimbaled MV x-ray head tracking system and acquiring experimental data. This research was funded by the Japan Society for the Promotion of Science (JSPS) through the Funding Program for World-Leading Innovative R&D on Science and Technology (FIRST Program), initiated by the Council for Science and Technology Policy (CSTP).

REFERENCES

1. P. J. Keall, G. S. Mageras, J. M. Balter, R. S. Emery, K. M. Forster, S. B. Jiang, J. M. Kapatoes, D. A. Low, M. J. Murphy, B. R. Murray, C. R. Ramsey, M. B. Van Herk, S. S. Vedam, J. W. Wong, and E. Yorke, "The management of respiratory motion in radiation oncology report of AAPM task group 76," Med. Phys. **33**, 3874–3900 (2006).
2. S.D. McCarter, and W.A. Beckham, "Evaluation of the validity of a convolution method for incorporating tumour movement and set-up variations into the radiotherapy treatment planning system," Phys. Med. Biol. **45**, 923–931 (2000).
3. T. Bortfeld, S. B. Jiang and E. Rietzel, "Effects of motion on the total dose distribution," Semin. Radiat. Oncol. **14**, 41–50 (2004).
4. F. M. Kong, R. K. T. Haken, M. J. Schipper, M. A. Sullivan, M. Chen, C. Lopez, G. P. Kalemkerian, and J. A. Hayman, "High-dose radiation improved local tumor control and overall survival in patients with inoperable/unresectable non-small-cell lung cancer: Long-term results of a radiation dose escalation study," Int. J. Radiat. Oncol. Biol. Phys. **63**, 324–333 (2005).
5. Y. Matsuo, K. Shibuya, M. Nakamura, M. Narabayashi, K. Sakanaka, N. Ueki, K. Miyagi, Y. Norihisa, T. Mizowaki, Y. Nagata, and M. Hiraoka, "Dose-volume metrics associated with radiation pneumonitis after stereotactic body radiation therapy for lung cancer," Int. J. Radiat. Oncol. Biol. Phys. In press (2012).
6. R. I. Whyte, R. Crownover, M. J. Murphy, D. P. Martin, T. W. Rice, M. M. DeCamp, R. Rodebaugh, M. S. Weihnous, and Q. T. Le, "Stereotactic radiosurgery for lung tumors: preliminary report of a phase I trial," Ann. Thorac. Surg. **75**, 1097–1101 (2003).

7. Y. Kamino, K. Takayama, M. Kokubo, Y. Narita, E. Hirai, N. Kawada, T. Mizowaki, Y. Nagata, T. Nishidai, and M. Hiraoka, “Development of a four-dimensional image-guided radiotherapy system with a gimbaled x-ray head,” Int. J. Radiat. Oncol. Biol. Phys. **66**, 271–278 (2006).

8. Y. Kamino, S. Miura, M. Kokubo, I. Yamashita, E. Hirai, M. Hiraoka and J. Ishikawa, “Development of an ultrasmall C-band linear accelerator guide for a four-dimensional image-guided radiotherapy system with a gimbaled x-ray head,” Med. Phys. **34**, 1797–1808 (2007).

9. A. Sawada, S. Kaneko, K. Takayama, K. Nagano, Y. Miyabe, M. Nakamura, Y. Narita, K. Takahashi, M. Kokubo, T. Mizowaki and M. Hiraoka, “Daily verification of isocenter alignment for a new image guided radiotherapy system, MHI-TM2000,” Med. Phys. **36**, 2586–2587 (2009).

10. M. Nakamura, A. Sawada, Y. Ishihara, K. Takayama, T. Mizowaki, S. Kaneko, M. Yamashita, H. Tanabe, M. Kokubo and M. Hiraoka, “Dosimetric characterization of a multileaf collimator for a new four-dimensional image-guided radiotherapy system with a gimbaled x-ray head, MHI-TM2000,” Med. Phys. **37**, 4684–4691 (2010).

11. K. Takayama, T. Mizowaki, M. Kokubo, N. Kawada, H. Nakayama, Y. Narita, K. Nagano, Y. Kamino, and M. Hiraoka, “Initial validations for pursuing irradiation using a gimbals tracking system,” Radiother. Oncol. **93**, 45–49 (2009).

12. N. Mukumoto, M. Nakamura, A. Sawada, K. Takahashi, Y. Miyabe, K. Takayama, T. Mizowaki, M. Kokubo, and M. Hiraoka, “Geometric accuracy of the x-ray image-based dynamic tracking for a four-dimensional image-guided radiotherapy system with gimbals mechanism of MHI-TM2000 (Vero),” Med. Phys. **38**, 3477 (2011).

13. Y. Miyabe, A. Sawada, K. Takayama, S. Kaneko, T. Mizowaki, M. Kokubo, and M. Hiraoka, “Positioning accuracy of a new image-guided radiotherapy system,” Med. Phys. **38**, 2535–2541 (2011).
14. T. Depuydt, D. Verellen, O. Haas, T. Gevaert, N. Linthout, M. Duchateau, K. Tournel, T. Reynders, K. Leysen, M. Hoogeman, G. Storme, and M. De Ridder, “Geometric accuracy of a novel gimbals based radiation therapy tumor tracking system,” Radiat. Oncol. **98**, 365–372 (2011).
15. N. Levinson, “The Wiener RMS (Root Mean Square) error criterion in filter design and prediction,” J. Math. Phys. **25**, 261–278 (1947).
16. J. Durbin, “The fitting of time series models,” Rev. Inst. Int. Stat. **28**, 233–243 (1960).
17. H. Nakayama, T. Mizowaki, Y. Narita, and M. Hiraoka, “Development of a three-dimensionally movable phantom system for dosimetric verifications,” Med. Phys. **35**, 1643–1650 (2008).
18. I.T. Jolliffe, *Principal Component Analysis* (Springer-Verlag, 2nd edition, New York, 2002).
19. H. F. Kaiser, “The application of electronic computers to factor analysis,” Educ. Psychol. Meas. **20**, 141–151 (1960).
20. A. E. Lujan, E. W. Larsen, J. M. Balter, and R. K. T. Haken, “A method for incorporating organ motion due to breathing into 3D dose calculations,” Med. Phys. **26**, 715–720 (1999).
21. Y. D. Mutaf, J. A. Antolak, and D. H. Brinkmann, “The impact of temporal inaccuracies on 4DCT image quality,” Med. Phys. **34**, 1615–1622 (2007).
22. Y. Seppenwoolde, H. Shirato, K. Kitamura, S. Shimizu, M. van Herk, J. V. Lebesque,

and K. Miyasaka, “Precise and real-time measurement of 3D tumor motion in lung due to breathing and heartbeat, measured during radiotherapy,” Int. J. Radiat. Oncol. Biol. Phys. **53**, 822–34 (2002).

23. P. J. Keall, H. Cattell, D. Pokhrel, S. Dieterich, K. H. Wong, M. J. Murphy, S. Vedam, K. Wijesooriya, and R. Mohan, “Geometric accuracy of a real-time target tracking system with dynamic multileaf collimator tracking system,” Int. J. Radiat. Oncol. Biol. Phys. **65**, 1579–1584 (2006).
24. B. Cho, P. R. Poulsen, A. Sloutsky, A. Sawant, and P. J. Keall, “First demonstration of combined kV/MV image-guided real-time dynamic multileaf-collimator target tracking,” Int. J. Radiat. Oncol. Biol. Phys. **74**, 859–867 (2009).
25. A. Sawant, R. L. Smith, R. B. Venkat, L. Santanam, B. Cho, P. Poulsen, H. Cattell, L. J. Newell, P. Parikh, and P. J. Keall, “Toward submillimeter accuracy in the management of intrafraction motion: the integration of real-time internal position monitoring and multileaf collimator target tracking,” Int. J. Radiat. Oncol. Biol. Phys. **74**, 575–582 (2009).
26. B. Cho, P. R. Poulsen, A. Sawant, D. Ruan, and P. J. Keall, “Real-time target position estimation using stereoscopic kilovoltage/megavoltage imaging and external respiratory monitoring for dynamic multileaf collimator tracking,” Int. J. Radiat. Oncol. Biol. Phys. **79**, 269–278 (2011).
27. R. D. Wiersma, N. Riaz, S. Dieterich, Y. Suh, and L. Xing, “Use of MV and kV imager correlation for maintaining continuous real-time 3D internal marker tracking during beam interruptions,” Phys. Med. Biol. **54**, 89–103 (2009).
28. W. Mao, N. Riaz, L. Lee, R. Wiersma, and L. Xing, “A fiducial detection algorithm for real-time image guided IMRT based on simultaneous MV and kV imaging,” Med.

Phys. **35**, 3554 (2008).

29. K. Wijesooriya, C. Bartee, J. V. Siebers, S. S. Vedam, and P. J. Keall, “Determination of maximum leaf velocity and acceleration of a dynamic multileaf collimator: implications for 4D radiotherapy,” Med. Phys. **32**, 932–941 (2005).
30. A. Schweikard, H. Shiomi, and J. Adler, “Respiration tracking in radiosurgery,” Med. Phys. **31**, 2738 (2004).
31. B. T. Collins, K. Erickson, C. A. Reichner, S. P. Collins, G. J. Gagnon, S. Dieterich, D. A. McRae, Y. Zhang, S. Yousefi, E. Levy, T. Chang, C. Jamis-Dow, F. Banovac, and E. D. Anderson, “Radical stereotactic radiosurgery with real-time tumor motion tracking in the treatment of small peripheral lung tumors,” Radiat. Oncol. **2**, 39 (2007).
32. H. C. Urschel, J. J. Kresl, J. D. Luketich, L. Papiez, and R. D. Timmerman, “Robotic radiosurgery. Treating tumors that move with respiration,” Germany, Berlin, New York, Springer, 265–282 (2007).
33. M. Hoogeman, J.-B. Prévost, J. Nuyttens, J. Pöll, P. Levendag, and B. Heijmen, “Clinical accuracy of the respiratory tumor tracking system of the cyberknife: assessment by analysis of log files,” Int. J. Radiat. Oncol. Biol. Phys. **74**, 297–303 (2009).
34. K. Malinowski, T. J. McAvoy, R. George, S. Dietrich, and W. D. D’Souza, “Incidence of changes in respiration-induced tumor motion and its relationship with respiratory surrogates during individual treatment fractions,” Int. J. Radiat. Oncol. Biol. Phys. In press (2011).
35. K. Takayama, N. Kawada, K. Nagano, Y. Sato, Y. Matsuo, T. Mizowaki, M. Kokubo, H. Nakayama, Y. Narita, and M. Hiraoka, “Imaging dose on a dual on-board kV x-ray

imaging system in MHI-TM2000," Int. J. Radiat. Oncol. Biol. Phys. **72**, S655–S656 (2008).

36. M. J. Murphy, J. Balter, S. Balter, J. A. BenComo, I. J. Das, S. B. Jiang, C. M. Ma, G. H. Olivera, R. F. Rodebaugh, K. J. Ruchala, H. Shirato, and F. F. Yin, "The management of imaging dose during image-guided radiotherapy: report of the AAPM Task Group 75," Med. Phys. **34**, 4041–4063 (2007).
37. M. K. Islam, T. G. Purdie, B. D. Norrlinger, H. Alasti, D. J. Moseley, M. B. Sharpe, J. H. Siewerdsen, and D. A. Jaffray, "Patient dose from kilovoltage cone beam computed tomography imaging in radiation therapy," Med. Phys. **33**, 1573–1582 (2006).
38. C. L. Perkins, T. Fox, E. Elder, D. A. Kooby, C. A. Staley, and J. Landry, "Image-guided radiation therapy (IGRT) in gastrointestinal tumors," J. O. P. **7**, 372–381 (2006).

FIGURE LEGENDS

Figure 1. Photograph of an x-ray image-based dynamic tumor-tracking irradiation system. The system comprised a 3D moving phantom with a steel ball target, a laser displacement gauge, an orthogonal kV x-ray imaging subsystem, consisting of two sets of x-ray tubes and flat-panel detectors, a gimbaled MV x-ray head, and the system controller of the vero4DRT. The gimbaled MV x-ray head enables rotation along the pan and tilt directions to track target motion, indicated by the imaging subsystem, while the laser displacement gauge synchronously measured the target motion in real time.

Figure 2. Schematic diagram showing (a) data flow to demonstrate the x-ray image-based dynamic tumor-tracking irradiation system and (b) geometric point of the tracked target position, indicated by the gimbaled MV x-ray head with a tilt rotation angle of θ°. The predicted, measured, and tracked positions of the target were recorded in the system controller. The tracked target position was calculated from the rotation angle of the gimbaled MV x-ray head. The difference between the target positions predicted by the sequential prediction model and those measured by the laser displacement gauge was computed as prediction error (E_P), and the difference between the target positions tracked by the gimbaled MV x-ray head and predicted target position as mechanical error (E_M). Total tracking system error (E_T) was derived from E_M and E_P, computed as the difference between the target positions tracked by the gimbaled MV x-ray head and those measured by the laser displacement gauge.

Figure 3. Variations in the measured and tracked positions of the target for sinusoidal

patterns with (a) (peak-to-peak amplitude [A], breathing period [T]) = (40 mm, 2 s), (b) (A, T) = (20 mm, 4 s), and circular patterns with (c) (A, T) = (40 mm, 2 s), and (d) (A, T) = (20 mm, 5 s). Solid lines show the measured positions of the target indicated by the laser displacement gauge, dashed lines show the tracked positions of the target indicated by the gimbaled MV x-ray head, and dotted lines show total tracking system errors (E_T), expressed as the differences between the tracked and measured positions of the target.

Figure 4. Variations in the measured and tracked positions of the target for (a) regular and (b) irregular respiratory cases. Solid lines indicate the measured positions of the target indicated by the laser displacement gauge, dashed lines show the tracked positions of the target indicated by the gimbaled MV x-ray head, and dotted lines show total tracking system errors (E_T). Probability histograms as a function of the alignment error between the target and gimbaled MV x-ray head with or without tracking are shown for (c) regular and (d) irregular respiratory cases, respectively. Solid lines show the alignment error with tracking, and dashed lines the alignment error without tracking.

Figure 5. Variations in the tracking efficiency, defined as the ratio of twice the root mean square of E_T ($RMSE_T$) to the peak-to-peak amplitude (A), as a function of principal component scores of patient respiratory motion. A strong positive correlation was observed between tracking efficiency and the principal component score ($R = 0.91$; $p < 0.01$).

Figure 6. Schematic diagram of the simulation and variations of the simulated dosimetric error of mean dose in planning target volume (PTV) under the conditions of the

displacements along the beam axis. The PTVs of 30 mm in diameter located at the displacements of -5, 0, and 5 mm from the isocenter with source-to-isocenter distance of 1000 mm were simulated under the condition of the one uniform field port adding 5-mm MLC margin. Dose calculation was performed under the same monitor unit with variance of 1% and a grid size of 2.3 x 2.3 x 2.5 mm^3 using X-ray Voxel Monte Carlo of well-commissioned 6 MV photon beam on a radiation treatment planning system (iPlan; BrainLAB, Germany).

TABLES

TABLE I. Characteristics of the motion patterns

		Sinusoidal (n = 4)	Circular (n = 3)	Respiratory (n = 15)
A [mm]	3D	20.0–40.0	20.0–40.0	6.5–22.9
	SI	20.0–40.0	20.0–40.0	6.0–19.5
	LR	0.0	20.0–40.0	1.5–10.7
	AP	0.0	0.0	1.0–11.3
T [s]		2.0–4.0	2.0–5.0	1.9–5.8

Abbreviations: A = peak-to-peak amplitude, T = breathing period, 3D = three-dimensional direction, SI = superior–inferior direction, LR = left–right direction, AP = anterior–posterior direction.

TABLE II. Root mean squares of the E_P, E_M, and E_T for sinusoidal and circular patterns

Case No.	*A* [mm]	*T* [s]	E_P [mm]	E_M [mm]	E_T [mm]
S1	40.0	2.0	0.8	0.3	0.7
S2	40.0	4.0	0.2	0.2	0.2
S3	20.0	2.0	0.4	0.2	0.4
S4	20.0	4.0	0.2	0.1	0.2
C1	40.0	2.0	0.2	0.3	0.2
C2	40.0	5.0	0.2	0.1	0.2
C3	20.0	5.0	0.2	0.1	0.2

Abbreviations: S* = sinusoidal pattern no.*, C* = circular pattern no.*, *A* = peak-to-peak amplitude, *T* = breathing period, E_P = prediction error, E_M = mechanical error, E_T = total tracking system error.

555

TABLE III. Motion characteristics and root mean squares of the E_P, E_M, and E_T for respiratory patterns

Case No.	*A* [mm]		*T* [s]		*AC*	E_P [mm]	E_M [mm]	E_T [mm]
	Mean	SD	Mean	SD				
1	7.9	1.5	2.9	0.4	0.72	1.0	0.1	1.0
2	22.9	5.6	5.8	0.9	0.67	1.3	0.1	1.3
3	18.2	6.3	4.7	0.7	0.66	1.2	0.1	1.2
4	18.8	6.3	5.3	1.8	0.57	1.3	0.1	1.3
5	13.8	5.7	4.5	0.6	0.68	1.1	0.1	1.1
6	19.4	2.7	4.9	0.6	0.89	0.9	0.1	1.0
7	19.0	3.2	4.6	0.8	0.72	1.0	0.1	1.0
8	21.3	2.4	5.3	0.3	0.92	0.9	0.1	0.9
9	15.1	5.0	4.6	0.6	0.79	1.2	0.1	1.2
10	17.4	7.0	4.9	1.0	0.73	1.4	0.1	1.5
11	17.2	4.9	4.4	0.8	0.85	1.0	0.1	1.0
12	6.5	2.3	1.9	0.2	0.59	1.2	0.1	1.2
13	14.5	1.9	4.5	0.9	0.74	1.4	0.1	1.4
14	19.6	2.0	3.2	0.5	0.81	1.8	0.2	1.8
15	17.5	5.6	3.6	0.7	0.56	1.8	0.5	1.8

Abbreviations: *A* = peak-to-peak amplitude, SD = standard deviation, *T* = breathing period, *AC* = autocorrelation coefficient with a lag of one breathing period, E_P = prediction error, E_M = mechanical error, E_T = total tracking system error.

560 **TABLE IV**. Principal component analysis for peak-to-peak amplitudes, breathing periods, and autocorrelation coefficients with a lag of one breathing period for 15 respiratory patterns

		1st principal component	2nd principal component	3rd principal component
Principal component coefficient	*A* [mm]	–0.919	–0.207	0.335
	T [s]	–0.900	–0.292	–0.324
	AC	–0.537	0.843	–0.030
Eigenvalue		1.94	0.84	0.22
Proportion		64.8	28.0	7.3
Accumulated proportion		64.8	92.7	100.0

Abbreviations: *A* = peak-to-peak amplitude, *T* = breathing period, *AC* = autocorrelation coefficient with a lag of one breathing period.

565 **TABLE V**. Comparison of the characteristics of dynamic tumor-tracking (DTT) irradiation techniques

	Present study		Cho *et al*.		Urschel *et al*.	Hoogeman *et al*.
Tracking mechanism	gimbaled head		dynamic MLC		robotic arm	
Monitoring system	kV + kV		kV + MV		kV + kV	
Monitoring dimension	3D		3D		3D	
Maximum field size	150 mm		depends on the installed linear accelerator		60 mm	
Motion type	1D or 2D periodic	3D aperiodic	3D aperiodic	3D aperiodic	1D periodic	3D aperiodic
Accuracy	0.2–0.7 mm	0.9–1.8 mm	< 1.5 mm *	< 2.5 mm **	1.1 mm	0.2–2.5 mm
Type of estimation	RMS	RMS	RMS	RMS	RMS	SD

Abbreviations: MLC = multileaf collimator, RMS = root mean square, SD = standard deviation.

*: accuracy excluding the prediction model building time period. **: accuracy including the prediction model building time period.

Figure 1

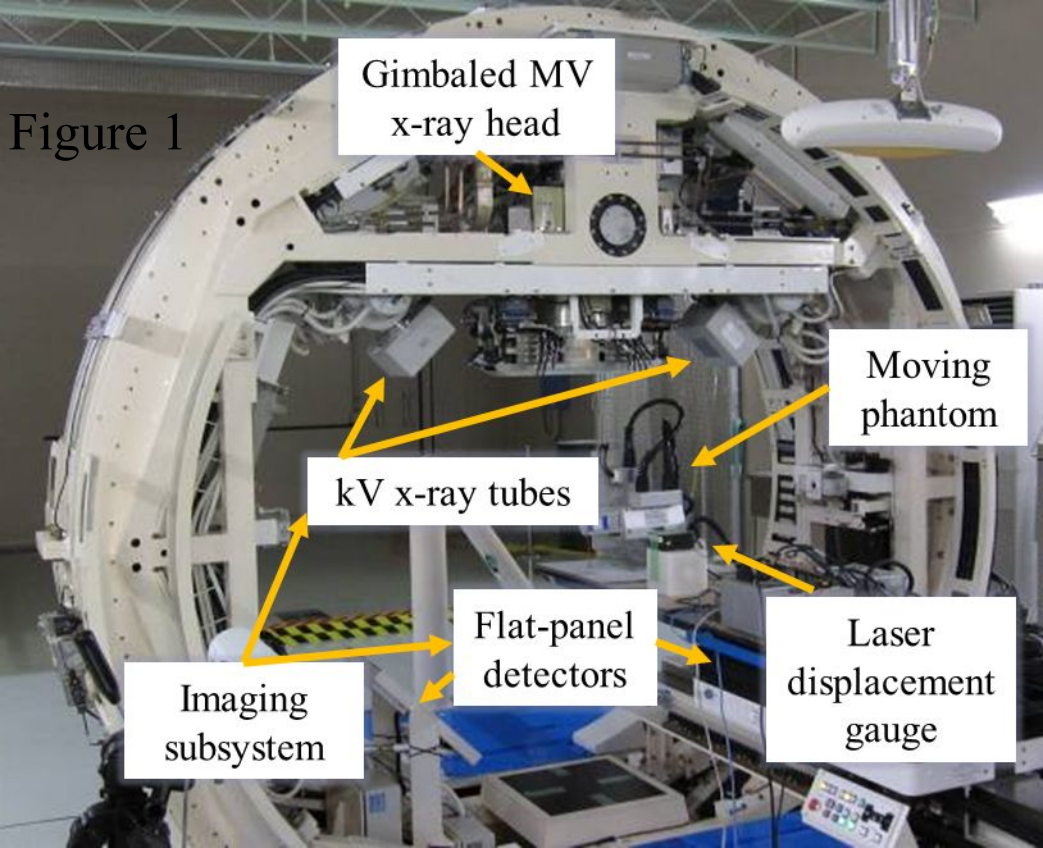
Gimbaled MV x-ray head
Moving phantom
kV x-ray tubes
Flat-panel detectors
Laser displacement gauge
Imaging subsystem

Figure 2a

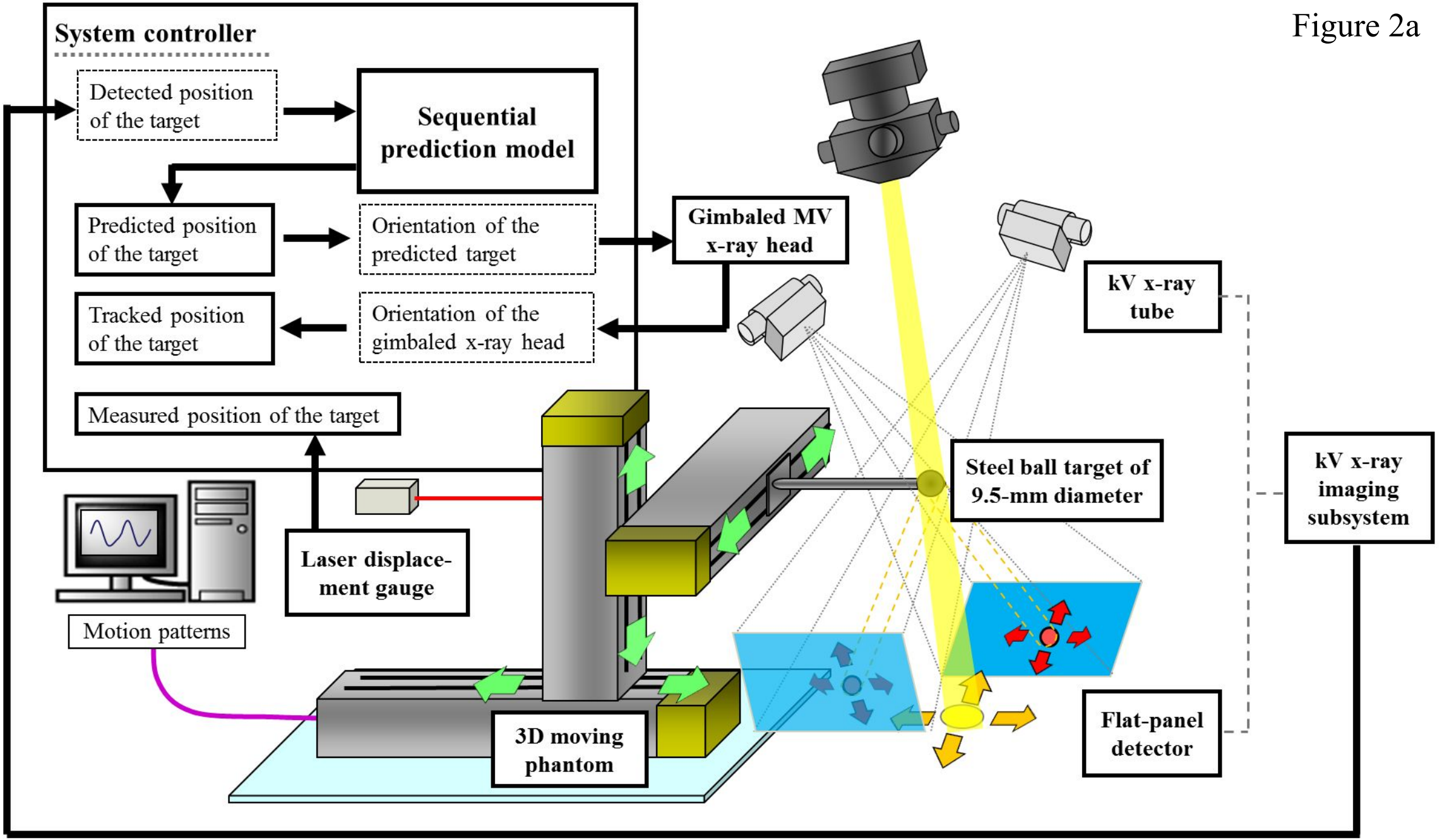
System controller
Detected position of the target
Sequential prediction model
Predicted position of the target
Orientation of the predicted target
Gimbaled MV x-ray head
Tracked position of the target
Orientation of the gimbaled x-ray head
Measured position of the target
kV x-ray tube
Steel ball target of 9.5-mm diameter
kV x-ray imaging subsystem
Laser displace-ment gauge
Motion patterns
3D moving phantom
Flat-panel detector

Figure 2b

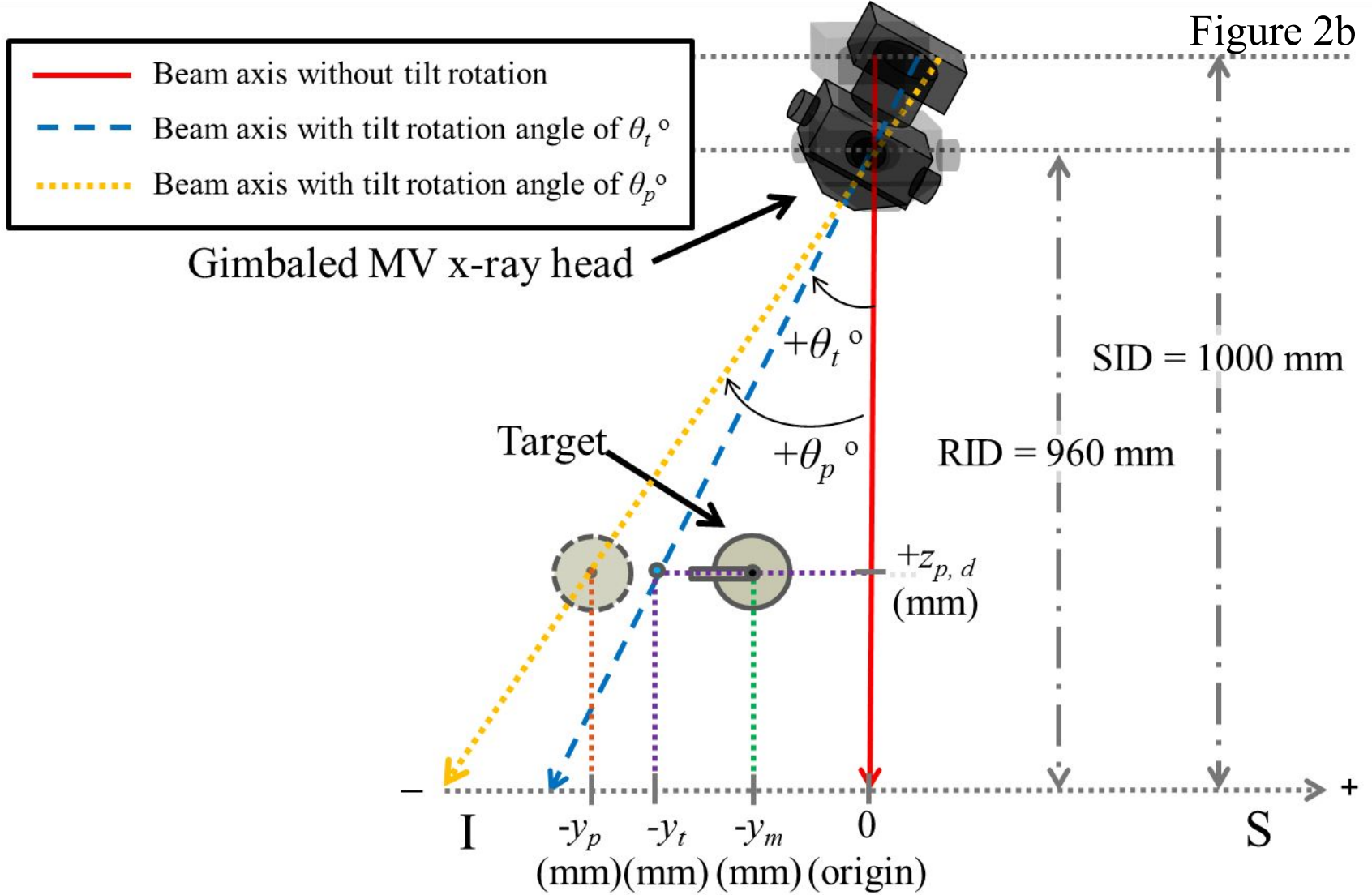

SID: source-to-isocenter distance, RID: head rotation center-to-isocenter distance

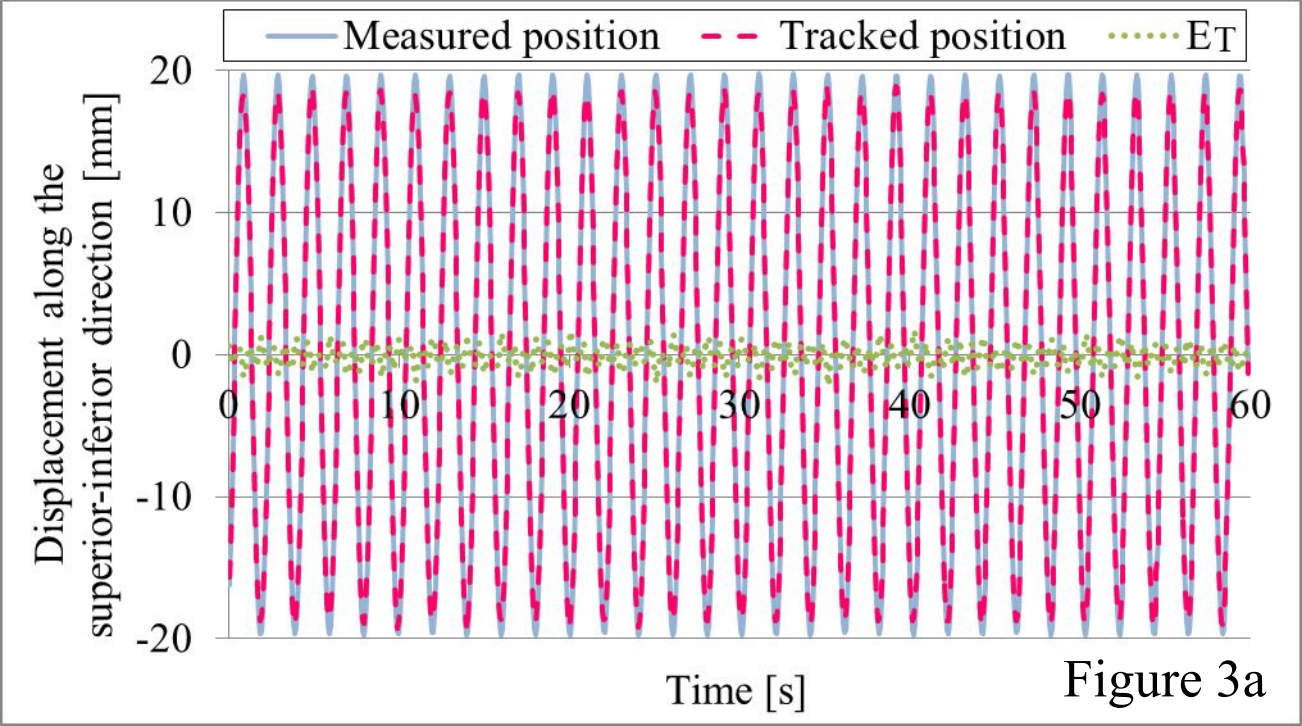
Measured position
Tracked position
ET
Displacement along the superior-inferior direction [mm]
20
10
0
-10
-20
0
10
20
30
40
50
60
Time [s]

Figure 3a

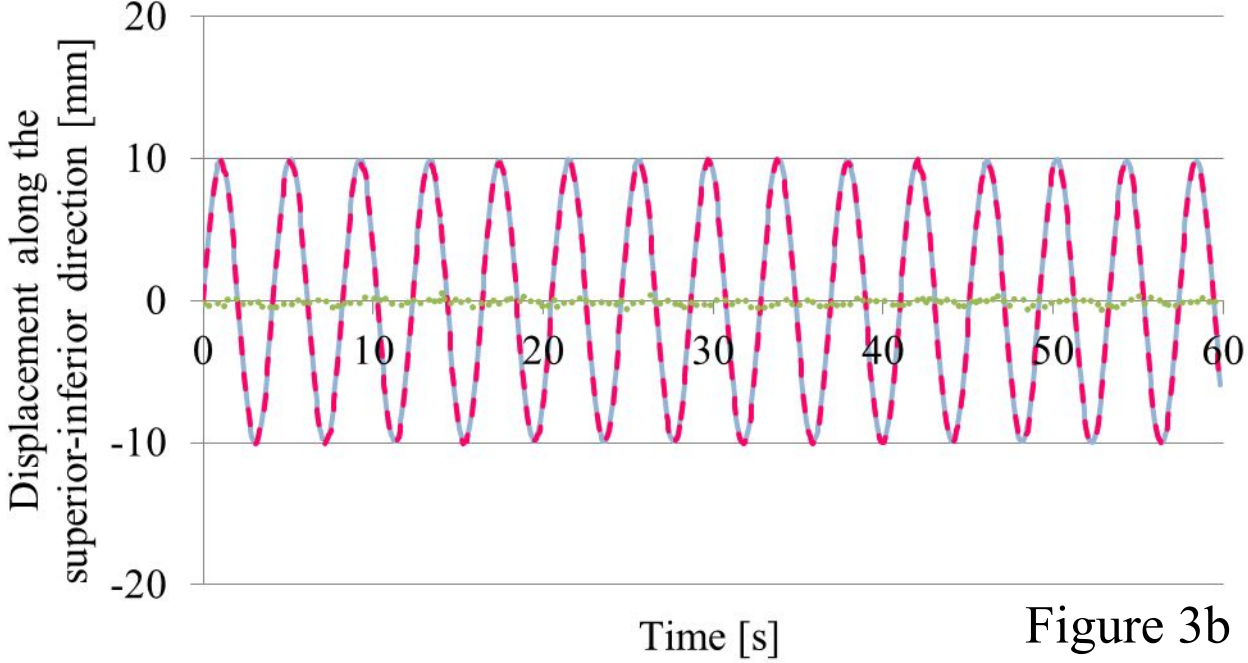
20
10
0
-10
-20
0
10
20
30
40
50
60
Displacement along the superior-inferior direction [mm]
Time [s]

Figure 3b

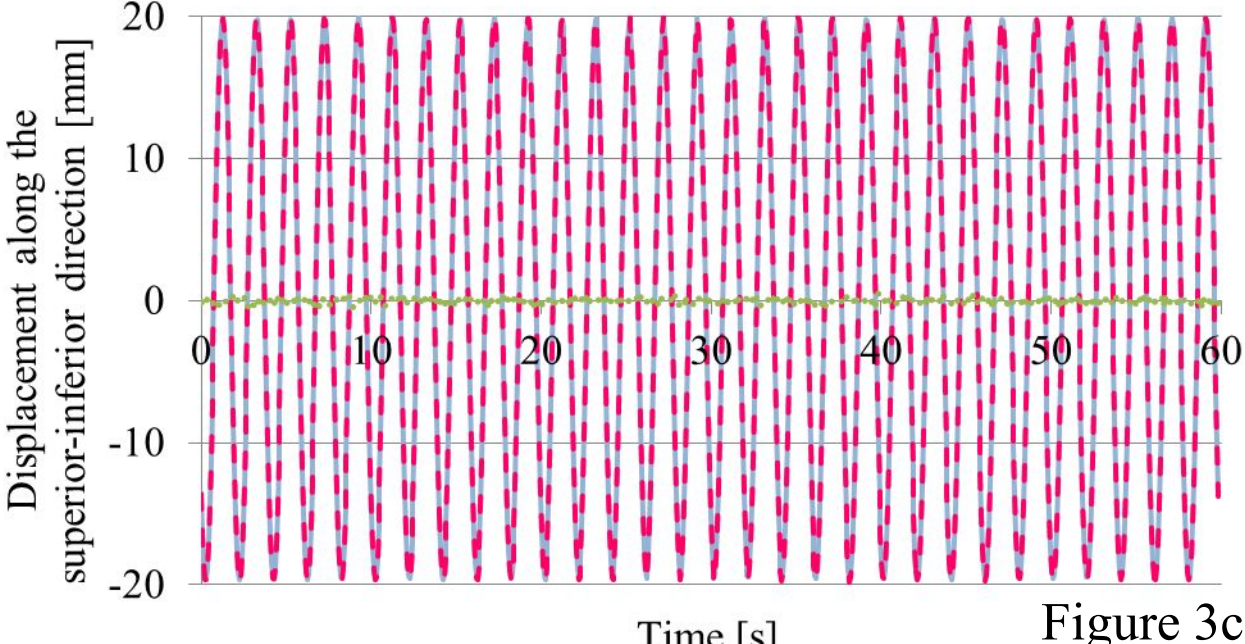
Displacement along the superior-inferior direction [mm]
20
10
0
-10
-20
0
10
20
30
40
50
60
Time [s]

Figure 3c

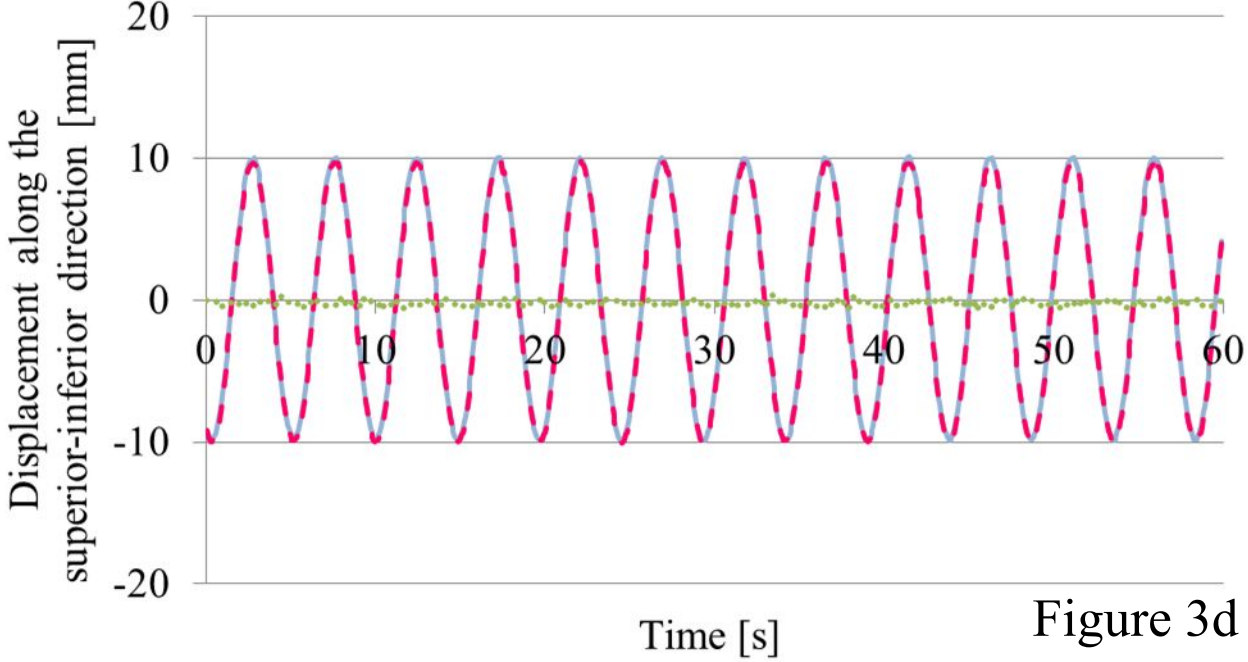
Displacement along the superior-inferior direction [mm]
20
10
0
-10
-20
0
10
20
30
40
50
60
Time [s]

Figure 3d

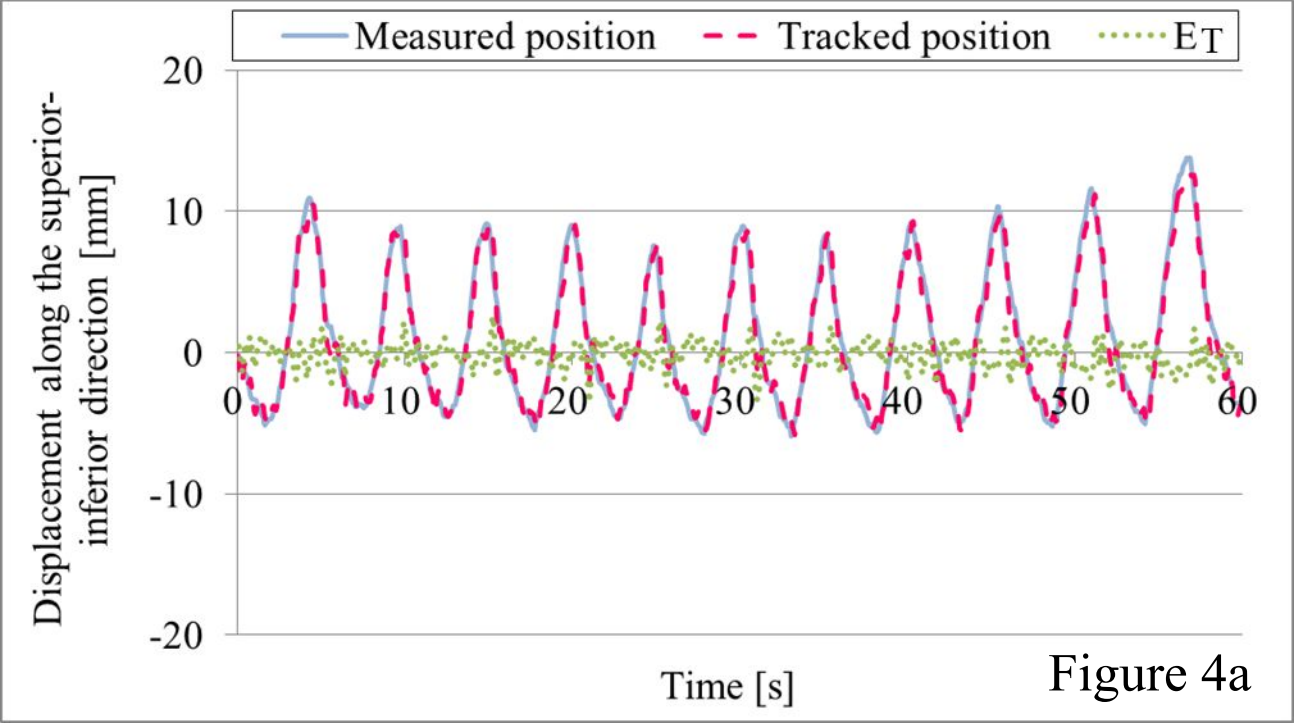
Measured position
Tracked position
ET
20
10
0
-10
-20
0
10
20
30
40
50
60
Displacement along the superior-inferior direction [mm]
Time [s]

Figure 4a

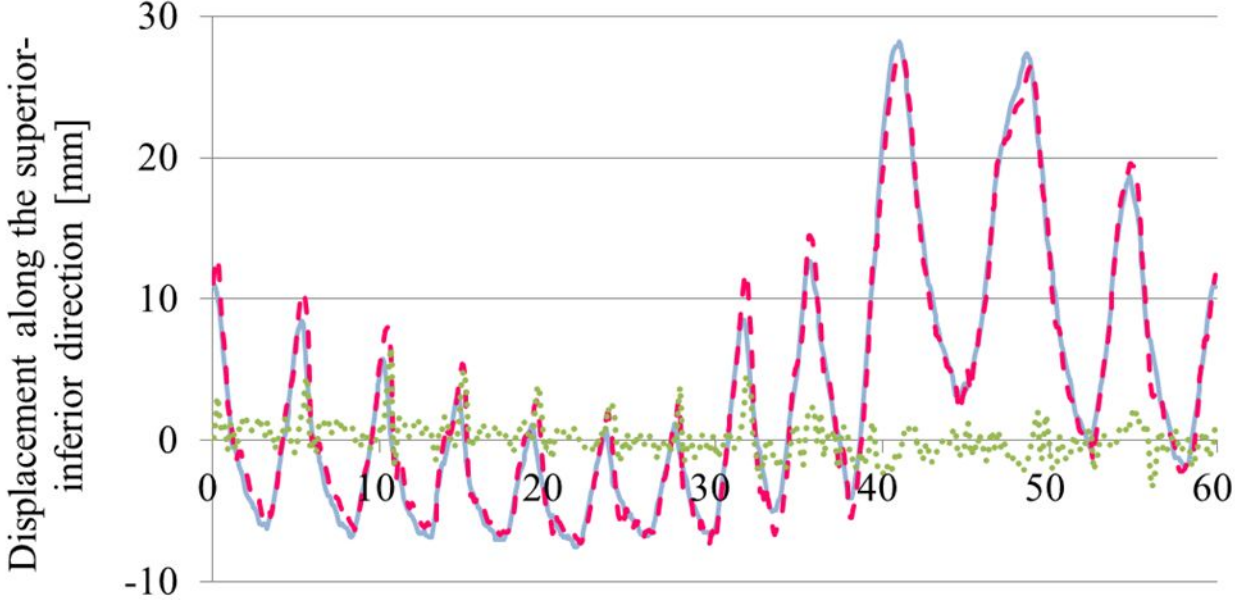
Displacement along the superior-inferior direction [mm]
30
20
10
0
-10
0
10
20
30
40
50
60
Time [s]

Figure 4b

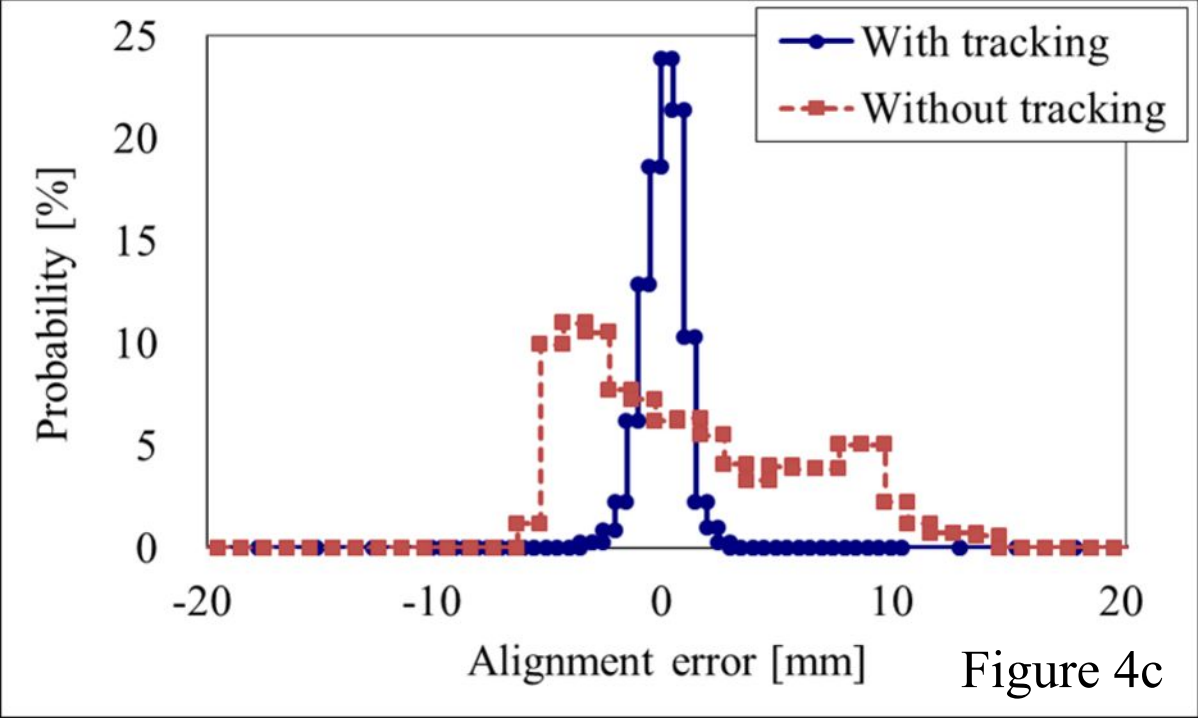
With tracking
Without tracking
Probability [%]
25
20
15
10
5
0
-20
-10
0
10
20
Alignment error [mm]

Figure 4c

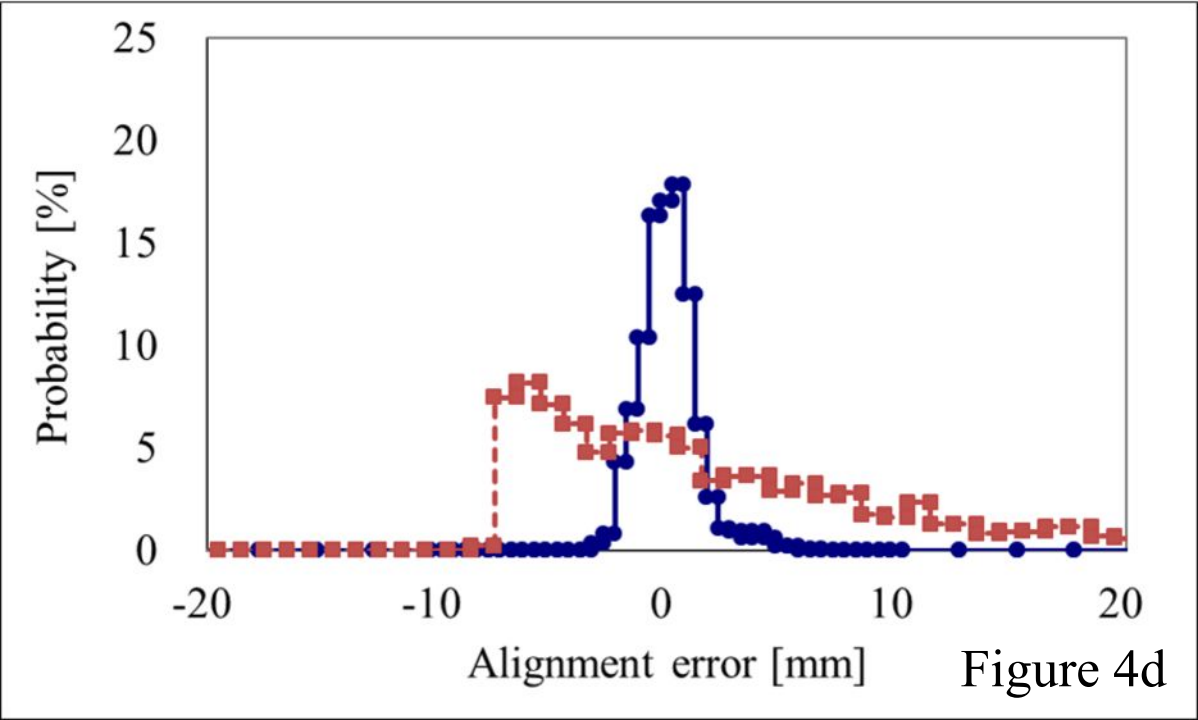

Figure 4d

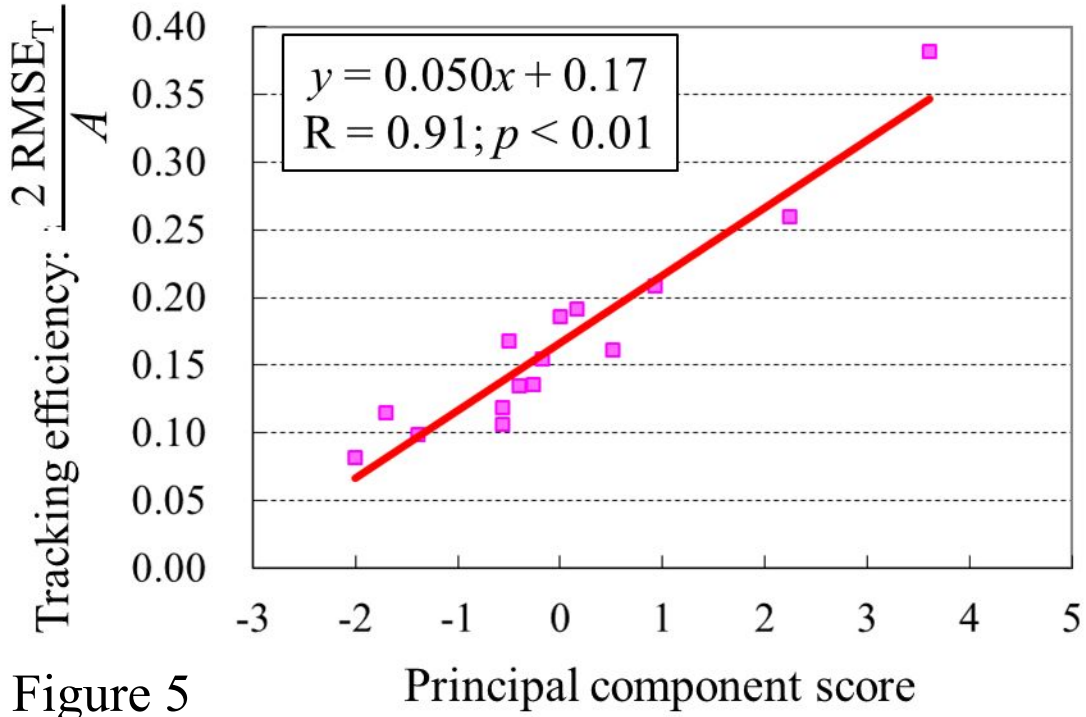
$y = 0.050x + 0.17$
R = 0.91; $p < 0.01$
Tracking efficiency: $\frac{2\ \mathrm{RMSE_T}}{A}$
0.40
0.35
0.30
0.25
0.20
0.15
0.10
0.05
0.00
-3
-2
-1
0
1
2
3
4
5
Principal component score

Figure 5

Figure 6

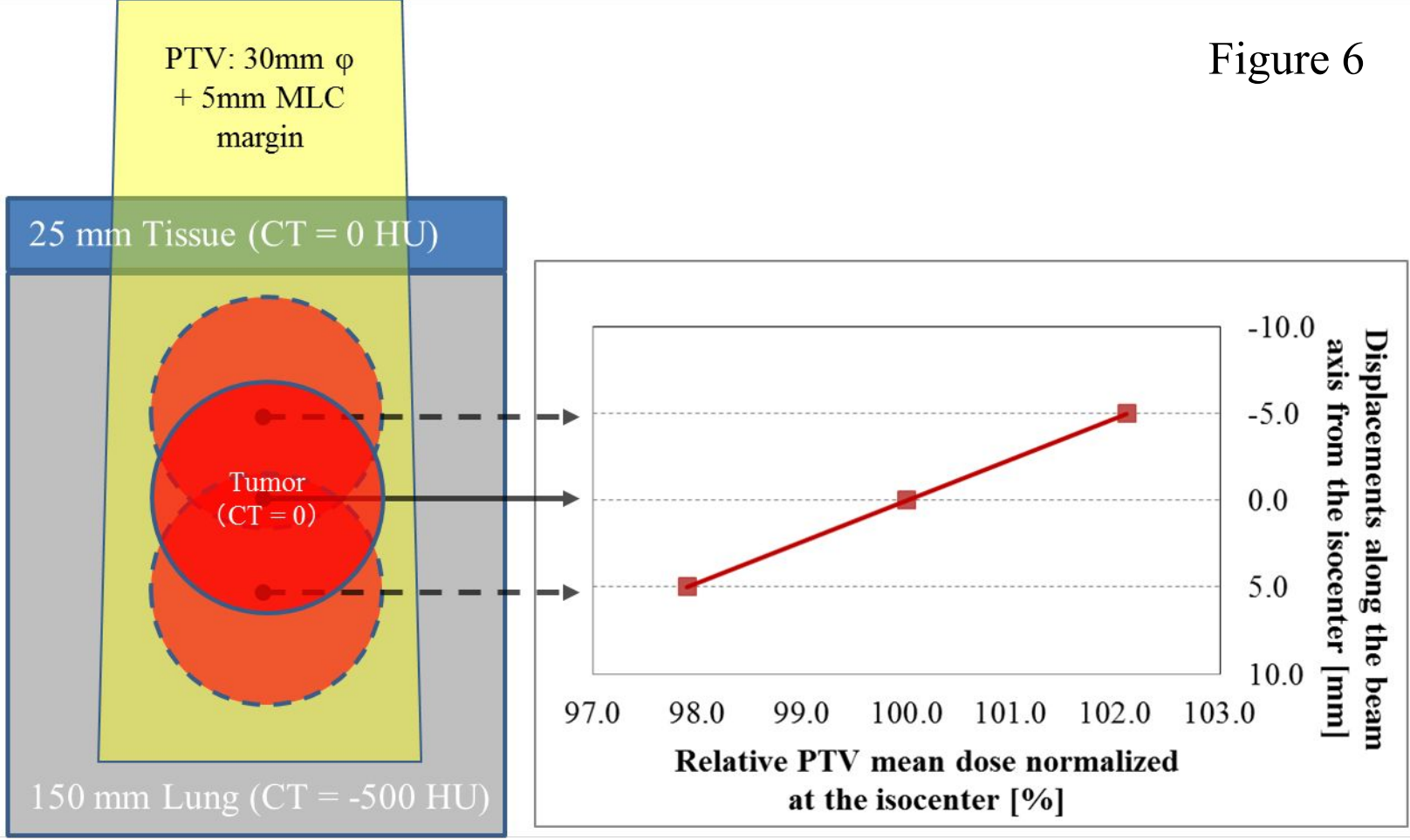
PTV: 30mm φ
+ 5mm MLC
margin
25 mm Tissue (CT = 0 HU)
Tumor
(CT = 0)
150 mm Lung (CT = -500 HU)
-10.0
-5.0
0.0
5.0
10.0
Displacements along the beam axis from the isocenter [mm]
97.0
98.0
99.0
100.0
101.0
102.0
103.0
Relative PTV mean dose normalized at the isocenter [%]